PHYSICAL REVIEW A, VOLUME 61, 063405

Imaging atomic Stark spectra

S. N. Pisharody, J. G. Zeibel, and R. R. Jones
Department of Physics, University of Virginia, Charlottesville, Virginia 22901

(Received 28 October 1999; published 8 May 2000)

Photoabsorption spectra have been measured as a continuous function of energy and applied electric field for the $m=0$, 1, and 2 Rydberg series in sodium. The spectra are Fourier transformed in scaled coordinates, generating scaled recurrence maps. The continuous nature of the scaled maps allows us to investigate patterns in the recurrence strength with good resolution.

PACS number(s): 32.60.+i, 32.80.Rm, 39.30.+w

I. INTRODUCTION

Electron dynamics in the presence of strong static electric fields continues to be a topic of considerable interest in atomic physics. The large spatial extent of Rydberg atoms makes them extremely sensitive to applied fields and, therefore, particularly interesting in this context. The dynamics of nonhydrogenic Rydberg electrons in the presence of the static field depend greatly on the relative strengths of the average Coulomb binding field and the applied electric field as well as the size of the non-Coulombic parts of the binding potential. In the frequency domain, these quantities determine the relative sizes of the energy splittings between (i) states of different principal quantum number $n, \Delta E_n \simeq 1/n^3$; (ii) states of different parabolic quantum numbers $k, \Delta E_k \simeq 3Fn$; and (iii) states with different Stark shifts undergoing avoided level crossings, ΔE_x. We use atomic units throughout and assume $n \gg 1$. In the time domain, the important time scales are the inverse of the energy splittings noted above: $\tau_{Kepler}=2\pi n^3$ is the time required for a classical Rydberg atom to move from the nucleus to the outer turning point of the radial potential and back; $\tau_{Stark}=2\pi/3Fn$ is the time required for the angular momentum of a classical electron to precess in the field from its initial value through all possible values and back; and $2\pi/\Delta E_x$ is the time required for an electron in a classical orbit aligned with the field to scatter into an orbit aligned opposite to the field due to precession of the Runge-Lenz vector in the non-Coulombic potential [1].

While experimental [2,3] and theoretical [4] time and frequency domain studies on this subject abound, relatively few provide a comprehensive quantitative view of the electron dynamics within a specific atom due to the large parameter space that must be investigated [5]. We have applied an imaging detection system to collect frequency domain photoabsorption spectra as a continuous function of excitation energy and static electric field. We have used Fourier transform analysis of the two-dimensional spectra to identify features in the global dynamics.

In the experiment, an entire Stark map is measured. Each map is a landscape of photoabsorption strength as a function of excitation energy and applied electric field [6]. The map can also be presented using ‘‘scaled variables,’’ namely, scaled energy and scaled action [7]. Scaled energy is defined as the quantity $\epsilon = EF^{-1/2}$ where E is the energy relative to the zero field ionization limit and F is the applied electric field in atomic units. Scaled action is the Fourier transform variable conjugate to $\omega = F^{-1/4}$. This scaling is based on transformation properties of the classical Hamiltonian of a hydrogen atom in an electric field, which can be written in cylindrical coordinates as

$$H=\frac{1}{2}(p_z^2+p_\rho^2)-\frac{1}{\sqrt{\rho^2+z^2}}+Fz. \tag{1}$$

After multiplication by $F^{-1/2}$ and the following change of variables,

$$\hat{\rho}=\rho F^{1/2}, \quad \hat{z}=zF^{1/2}, \tag{2}$$

$$\hat{p}_\rho=p_\rho F^{-1/4}, \quad \hat{p}_z=p_z F^{-1/4}, \tag{3}$$

$$\hat{t}=tF^{1/4}, \tag{4}$$

the Hamiltonian becomes

$$\hat{H}=HF^{-1/2}=\frac{1}{2}(\hat{p}_z^2+\hat{p}_\rho^2)-\frac{1}{\sqrt{\hat{\rho}^2+\hat{z}^2}}+\hat{z}. \tag{5}$$

This scaled Hamiltonian depends only on the scaled energy ϵ, and not on the applied field or excitation energy independently. For any given value of the scaled energy, the classical dynamics of the system do not depend independently on the binding energy and static field. The electron dynamics are revealed by Fourier transforming the photoabsorption strength I with respect to the scaled variable ω, at constant scaled energy ϵ. Resonance peaks in this ‘‘recurrence’’ spectrum are associated with electrons moving around the nucleus in classical periodic orbits that are closed at the atomic core [7,8].

Previous experiments in which electron dynamics were studied using recurrence spectroscopy have relied on simultaneous variation of the electric field and laser frequency to measure $I(\omega)$ at constant scaled energy [7,9–12]. Using this technique, identification of global trends in the spectra as a function of scaled energy is difficult, since typically only a small number of discrete scaled energy spectra can be measured in any reasonable amount of time. For example, Eichmann *et al.* looked at sodium spectra, but only for $\epsilon=-2.5$ [7]. Hogervorst and co-workers have studied the specific scaled energies of $\epsilon=-2.94$, -2.35, and -1.76 in great detail with good experimental accuracy in barium [10]. While their choices of scaled energies represent points both above and below the classical ionization limit ($\epsilon=-2.0$), the work does not provide complete information on the evo-

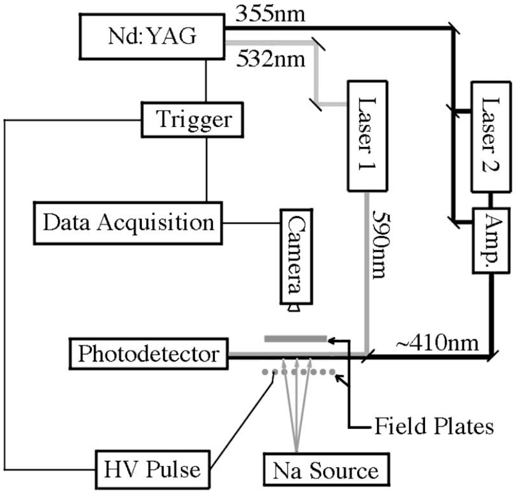

FIG. 1. A schematic representation of the experimental apparatus. Parallel wires connected through a resistor chain create a field gradient which enables spectroscopic measurements to be made over a continuous range of applied field.

lution of electron dynamics as a function of scaled energy. Courtney *et al.* [5,9] were the first to look for global patterns in experimental recurrence spectra. They measured photoabsorption spectra over a quasicontinuous range of scaled energies from $\epsilon = -2.6$ to $\epsilon = -4.0$ in steps of $\Delta\epsilon = 0.1$ [5]. They discovered recurrence maxima in their Li data that had no analog in computed hydrogen spectra. These features were attributed to combination orbits, apparently caused by scattering from the nonhydrogenic core. The work of Keeler and Morgan [12] in helium has come the closest to observing a recurrence spectrum that was continuous in scaled energy, with individual scaled energy scans separated by $\Delta\epsilon = 0.02$ from $\epsilon = -2.0$ to $\epsilon = -3.4$. From their recurrence maps, Keeler and Morgan identified combination orbits as well as a periodic modulation of the scaled-energy-integrated recurrence strengths within various sequences of resonance peaks corresponding to different periodic orbits [12].

While quantum simulations can reproduce the experimental data, much of the real insight into electron dynamics in external fields has come from classical and semiclassical analyses [1–4,7,8,13–15]. In particular, closed orbit theory has provided an elegant semiclassical explanation for the majority of the experimental results observed in recurrence spectroscopy [7,8]. The theory relates the observed maxima in the recurrence spectrum to the probability for launching an electron into a particular closed orbit. Despite its successes, the original theory, which assumed hydrogenic atoms, did not account for all of the observed features in the nonhydrogenic spectra [5,7,8]. In a modification of the theory, electrons incident on the nonhydrogenic core have a finite probability of being scattered into all possible orbits, leading to the observed ‘‘combination’’ peaks in the recurrence spectra [5,10,11]. However, current semiclassical theory has not yet reproduced all the details in measured nonhydrogenic recurrence spectra [5,10,11]. Shaw and Robicheaux have compared quantum scaled energy calculations with semiclassical closed orbit theory for H, K, and Cs [13]. They found slight deviations between the quantum and closed orbit calculations near the locations of recurrence maxima, which they were able to account for with a correction term. They also investigated patterns observed within a given recurrence maximum as a function of scaled energy, but did not identify any overall trends.

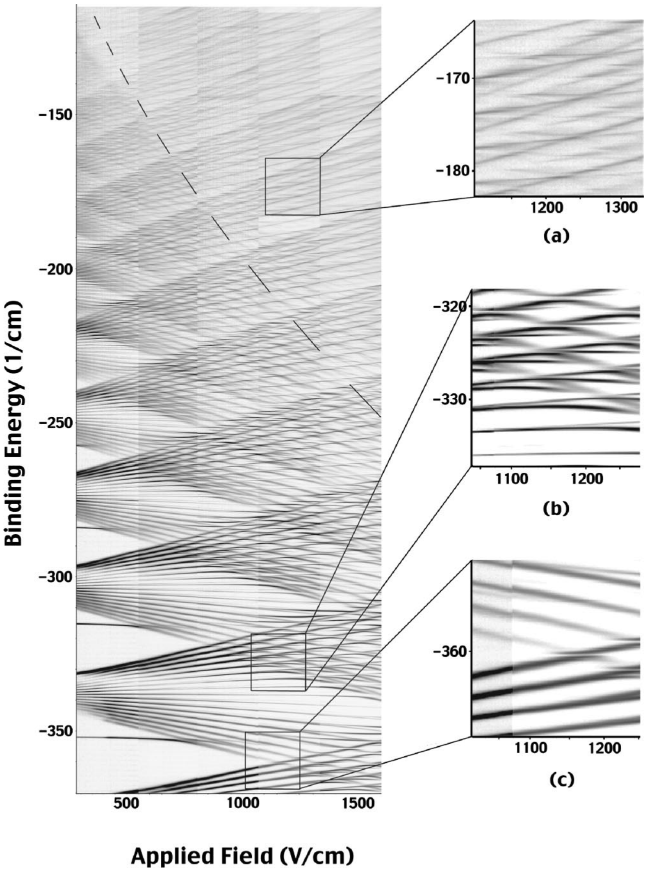

FIG. 2. Density plot of the measured Stark map of sodium for parallel field and laser polarization, $m = 0,1$. Dark regions represent high excitation probability. Expanded views of selected locations in the spectrum can be found in insets (a), (b), and (c). In particular, (c) shows the avoided crossing of the $n = 18$ downhill state with the $n = 17$ uphill state. Such crossings between the n and $n+1$ manifolds for $17 \leqslant n \leqslant 21$ are used as an absolute field calibration. The dashed line is the classical field ionization limit, $F = 1/16n^4$.

The goal of the work described here is to investigate variations in the recurrence strength as a continuous function of scaled energy and scaled action, thereby providing a better understanding of electron dynamics in a combined Stark-Coulomb system (in this case, the sodium atom). Recurrence spectra are collected over a range of scaled energies $-4.5 \leqslant \epsilon \leqslant -1.5$ and scaled actions $0 \leqslant S \leqslant 30$. In the following sections, we describe our experimental procedure and numerical analysis of the data. We introduce a set of modified scaled parameters that guides our interpretation of the data. We then compare our results with quantum simulations for Na and H. We conclude with a brief summary of our findings.

II. EXPERIMENTAL SETUP

Figure 1 shows a schematic of the experiment. Thermally excited Na atoms from a resistively heated oven interact with

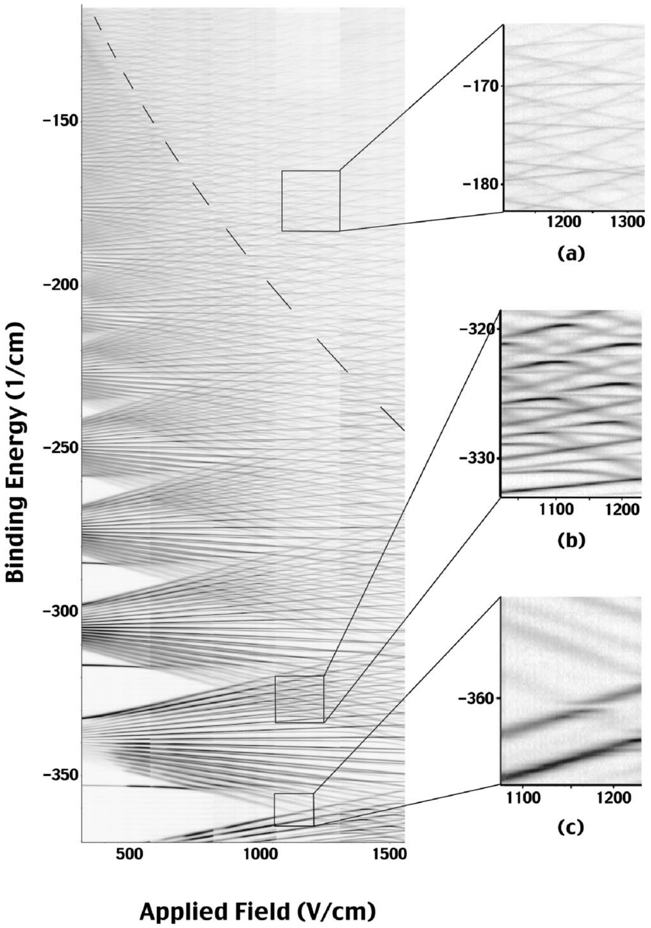

FIG. 3. Density plot of the measured Stark map for sodium for perpendicular field and second laser polarization, $m=0,1,2$. Dark regions represent high excitation probability. The $m=2$ features dominate the spectrum. Note that unlike the $m=0$ case, the $m=2$ oscillator strength is predominantly located in the center of each manifold. Therefore, the center manifold states are more visible in this figure than in the corresponding $m=0$ data in Fig. 2. Expanded views of selected locations in the spectrum can be found in insets (a), (b), and (c). The dashed line is the classical field ionization limit, $F=1/16n^4$.

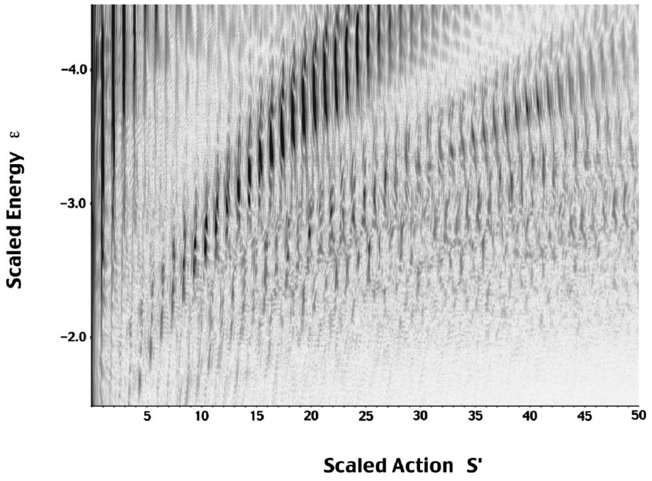

FIG. 4. Density plot of the measured scaled energy recurrence map of $m=0,1$ in sodium. The action axis used here differs by a factor of $\sqrt{2\epsilon}$ from those in previous studies. This action coordinate S' identifies the number of primary Kepler orbits. In contrast to previous work, the recurrence map represents the Fourier transform of the scaled data, not the square of the Fourier transform. This choice makes it easier to see small features in the recurrence strength.

two copropagating nanosecond dye lasers in a spatially inhomogeneous electric field. The two lasers are pumped at a 15 Hz repetition rate by the second and third harmonics of a Nd:YAG (where YAG is yttrium aluminum garnet) laser, respectively. The first laser excites the $3S$ ground state Na atoms to an intermediate $3P_{1/2}$, $|m_j|=\frac{1}{2}$ state. The second laser pulse is delayed relative to the first by ~5 ns and is linearly polarized either perpendicular or parallel to the applied electric field. The parallel and perpendicular polarizations allow for excitation of pure $|m_j|=\frac{1}{2}$ or $|m_j|=\frac{1}{2},\frac{3}{2}$ states, respectively. The frequency of the second dye laser is tunable, permitting the excitation of the $3P_{1/2}$ atoms to Rydberg states with principal quantum number $17\leqslant n\leqslant 30$. The second dye laser is in a double-grating Littman configuration [16] and it has a linewidth of 0.14 cm^{-1}. The spatially varying electric field is prepared using a parallel plate geometry with a voltage gradient along the lower field ''plate.'' The field gradient is produced by a set of 13 parallel wires in a resistor chain with a fixed voltage difference applied to the two ends of the chain. By keeping the distance between adjacent wires much smaller than the distance from the wires to the interaction region, the horizontal component of the electric field is minimized. The top field plate is 7.5 cm on a side. The lower plate wires are fixed 12 mm below the top plate and are each separated by 2 mm. The atomic beam enters the interaction region ~5 mm below the top plate.

Fifty nanoseconds following the Rydberg state excitation, a strong voltage pulse (~10 kV) is applied to all the wires in the resistor chain. Any Rydberg atoms produced by the laser are ionized either by the static field or by the voltage pulse. The resulting ions are accelerated toward a microchannel plate assembly through a 1.6 mm×25 mm slit in the top field plate. The microchannel plates generate electrons in di-

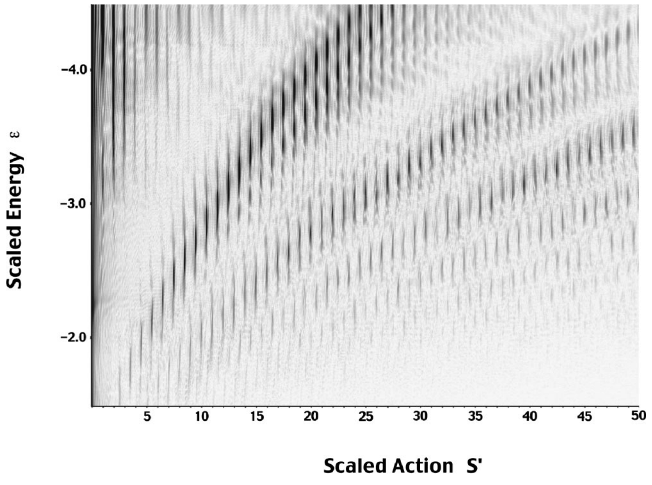

FIG. 5. Density plot of the measured scaled energy recurrence map of $m=2$ in sodium analogous to Fig. 4.

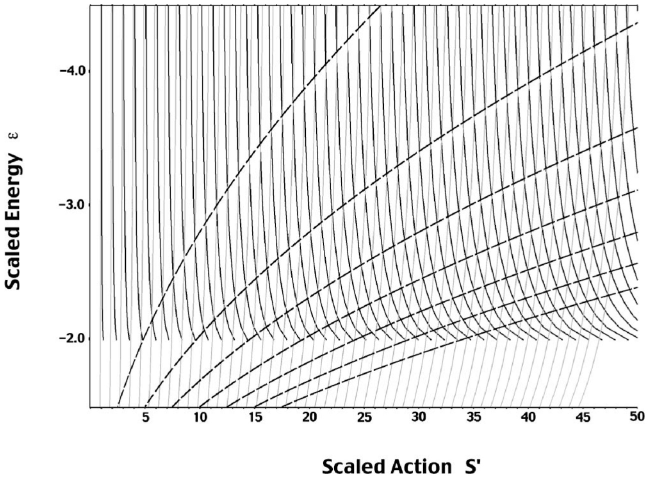

FIG. 6. Scaled actions of the primary hydrogenic uphill and downhill orbits and their repetitions as a function of scaled energy. The dark lines represent the uphill orbits, while the lighter lines represent the downhill orbits. To a good approximation, for $\epsilon < -2.5$, the ith repetition of the uphill orbit crosses the $(i+j)$th repetition of the downhill orbit at $S' = i + j/2$. The dashed curves are the expression $\epsilon = \sqrt{3(S' + j/2)/4j}$, which identifies the crossing of the ith downhill orbit with the $(i+j)$th uphill orbit. The approximate expression is valid for $\epsilon \lesssim -2.5$.

rect proportion to the number of incident ions, and these electrons are accelerated toward a phosphor screen that lies directly behind the microchannel plates. The electron-induced fluorescence from the phosphor is observed with a charge-coupled device (CCD) camera. The ionization yield as a function of position along the slit in the upper field plate is directly proportional to the excitation probability versus electric field. The range of electric fields present in the interaction region is determined by the difference in the voltages applied to the two ends of the lower ''plate'' resistor chain. To avoid severe nonlinearity in the field gradient, only signal originating beneath the central 50% of the extraction slit is used to generate the Stark map. The frequency of the second laser is scanned to generate a portion of a Stark map that is continuous in both energy and applied field.

In this experiment, each dye laser scan covers electron binding energies from $-114.5\ \mathrm{cm}^{-1}$ to $-371.2\ \mathrm{cm}^{-1}$ and a field range of approximately 300 V/cm. Five laser scans covering different field ranges are combined to produce a single Stark map over a field range from 300 V/cm to 1600 V/cm. Relative frequency calibration is achieved by monitoring the second laser transmission through a 2 mm solid étalon. The envelope of the maxima in the étalon fringe pattern is used as a normalization to correct for variations in laser intensity over the scans. Absolute frequency calibration is obtained from the known zero field s state energies. The electric field is calibrated using the theoretically calculated fields at the center of the avoided crossings of the reddest state of the $(n+1)$th manifold with the bluest state of the nth manifold for $17 \leqslant n \leqslant 21$. Figures 2(c) and 3(c) show the avoided crossing of the reddest state of the $n=18$ manifold with the bluest state of the $n=17$ manifold for parallel and perpendicular laser polarization, respectively. Relative field calibration is performed by tracking the position of a particular feature in the Stark map as the voltage offset applied to the resistor chain is varied.

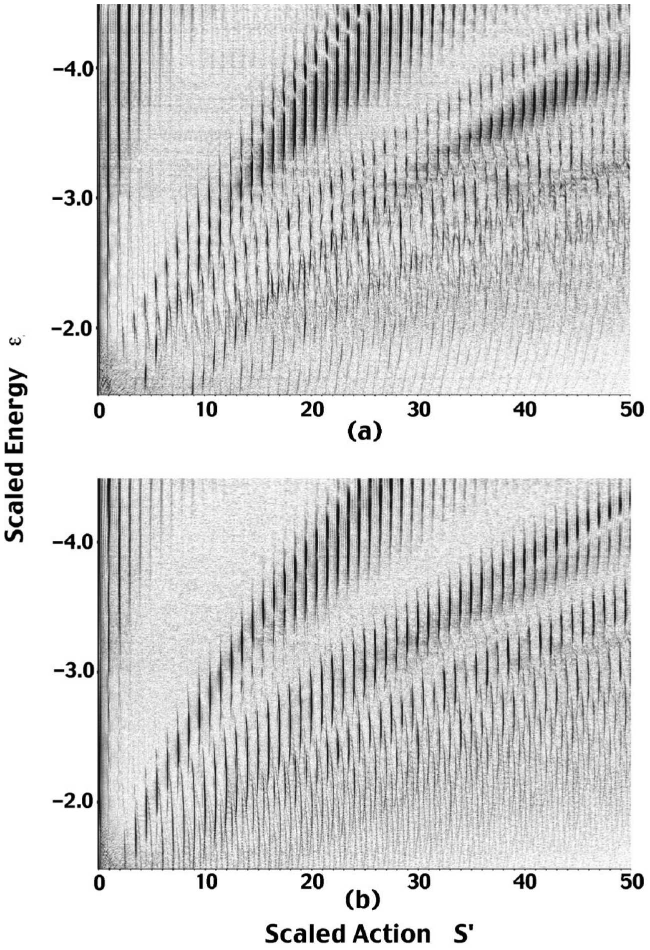

FIG. 7. Density plot of quantum calculations of the recurrence spectra of sodium. (a) shows the recurrence map with $m=0,1$ character weighted to match the experimental conditions for parallel laser polarization, while (b) shows the recurrence map with the $m=0,1,2$ characters weighted to match the perpendicular polarization case (primarily $m=2$).

Figures 2 and 3 show two Stark maps for parallel and perpendicular second laser polarization, respectively. While $m=0,1,2$ states contribute to the image in Fig. 3, the $m=2$ structure dominates. Henceforth we refer to Fig. 3 as the $m=2$ spectrum. In Fig. 2, the $m=0$ and 1 resonances have relative weights of 1:2. These Stark maps may be used to generate recurrence maps by rescaling the energy and field axes as described above, and Fourier transforming with respect to $\omega = F^{-1/4}$. However, we use a different method for displaying scaled spectroscopic data. Instead of Fourier transforming with respect to ω, we divide ω by the factor $\sqrt{2|\epsilon|}$, yielding $\omega' = 1/\sqrt{2|E|} = n^*$. Conversion to ω' before Fourier transforming serves two purposes. First, the dependence on field is removed from the new action coordinate S', eliminating uncertainties due to the field calibration or inhomogeneity. Second, in these units the strongest recurrences are localized at integer or half-integer values of the independent variable S'.

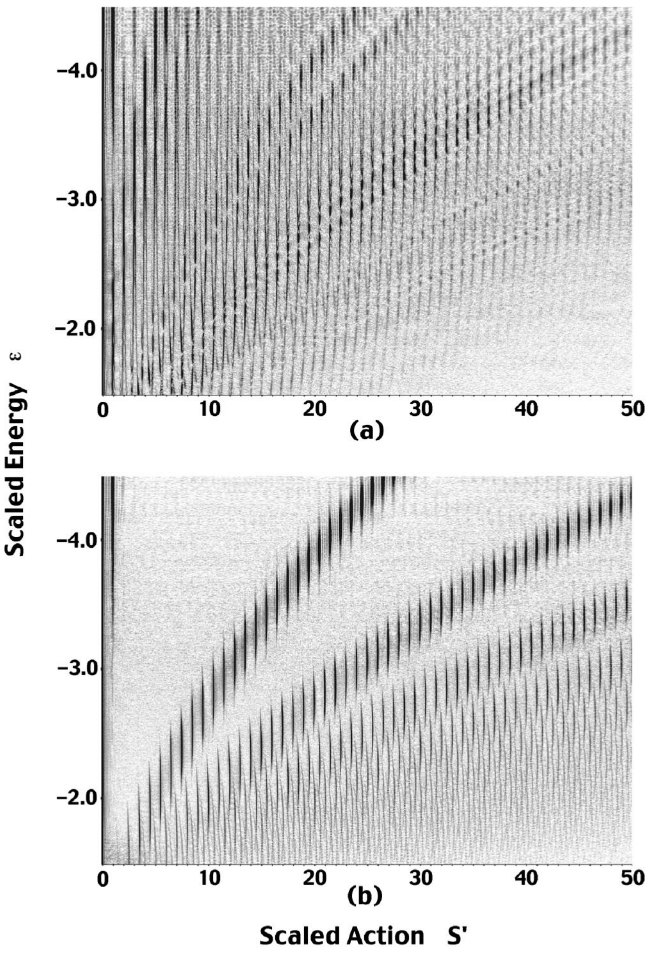

FIG. 8. Density plot of quantum theoretical calculations of the recurrence spectra in hydrogen. (a) shows the $m=0$ spectrum and (b) shows the $m=2$ spectrum.

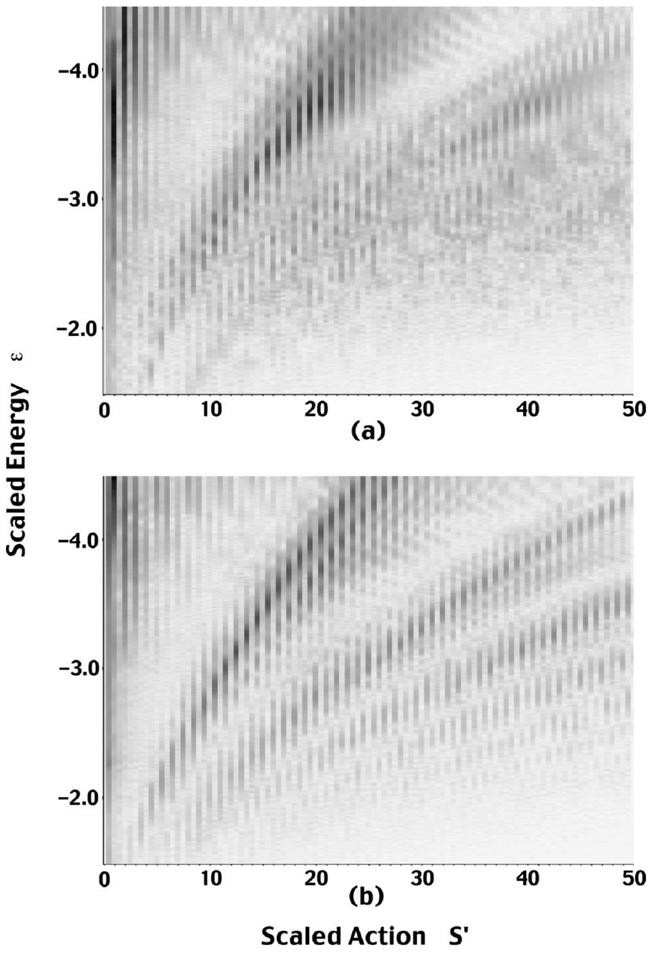

FIG. 9. Density plot of the experimental recurrence spectra of sodium with the area around each integer and half-integer value of scaled action integrated. (a) shows the recurrence map with $m=0,1$ character, while (b) shows the integrated recurrence map with mainly $m=2$ character.

The experimental results for $m=0,1$ (Fig. 4) and $m=2$ (Fig. 5) show clear sequences of recurrence maxima. The $m=2$ sequences are more separated and distinct than the corresponding sequences for $m=0,1$. The cross section for excitation of $m=2$ Stark spectra is larger near the center of the manifolds, while for $m=0$ the oscillator strength is peaked near the highest and lowest energy states in each Stark manifold. The Fourier transform of the $m=2$ data displays better resolved sequences in the recurrence map as the periodicity of the center of the Stark manifolds is quite evident. Successive manifolds are relatively unaffected by neighboring ones due to the small quantum defect of the higher m states. However, in the $m=0$, 1 spectra, neighboring Stark manifolds interact quite strongly due to the larger quantum defect. The strong intermanifold periodicity that was evident in the $m=2$ spectrum is not as pronounced.

In the $m=2$ recurrence map, peaks in recurrence strength occur at either integer or half-integer values of the action coordinate S'. Up to nine separate sequences of maxima are observed, each occurring for $S'=j$ or $S'=j+\frac{1}{2}$, for $j=1,2,3,\ldots$. To a good approximation, for $\epsilon<-2.5$, the $m=0,1$ spectra also show maxima located primarily at either integer or half-integer values of S'. Over this range of scaled energies, the actions of the ''uphill'' and ''downhill'' repetition orbits of hydrogen cross each other at integer or half-integer values of S' as well (see Fig. 6). Roughly, for $m=0,1$, the maxima in recurrence strengths occur when an uphill and downhill orbit share the same value of S'. Sequence I maxima occur at the intersection of the ith uphill and $(i+1)$th downhill repetition orbits. For $\epsilon<-2.5$ in sequence I, these crossings occur at $S'=(i+1/2)$. More generally, sequence j maxima appear at the intersection of the ith repetition of the uphill orbit with the $(i+j)$th repetition of the downhill orbit at $S'=i+j/2$. Figure 6 shows action versus scaled energy for the primary uphill and downhill orbits in hydrogen. It should be noted that for $\epsilon>-2.5$ the crossings of the uphill and downhill orbits and the associated maxima in the recurrence strength diverge from integer and half-integer values of S'.

III. ANALYSIS AND DISCUSSION

A. Theoretical simulations

Our experimental results can be compared to full quantum simulations. Quantum-mechanical calculations of the Stark

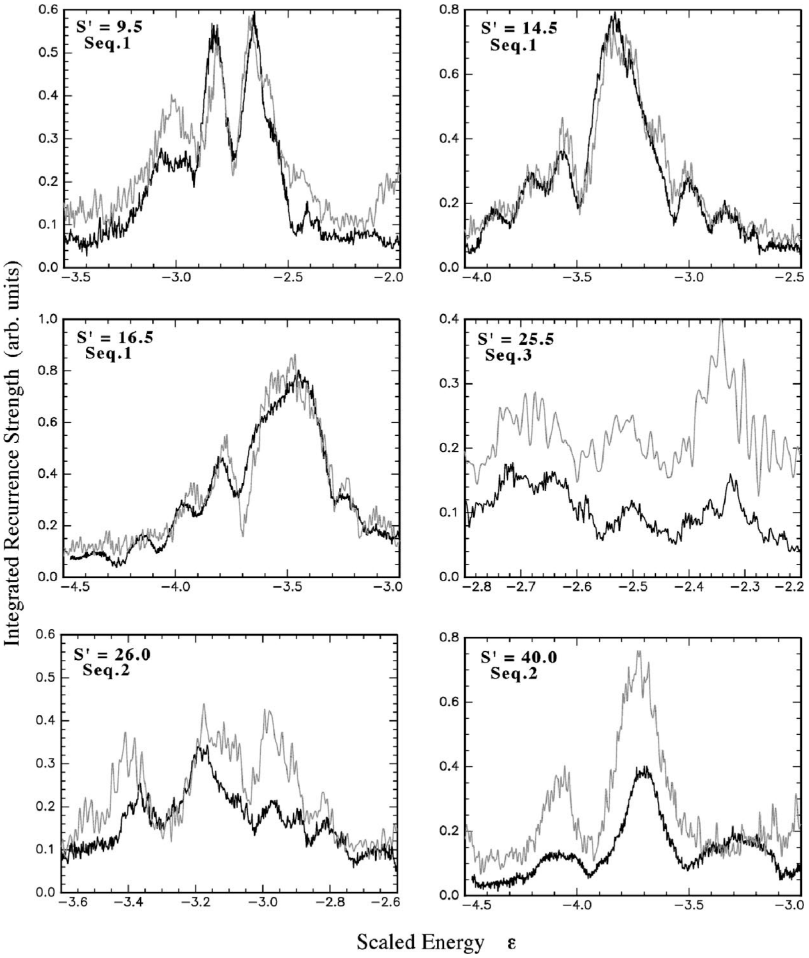

FIG. 10. Comparison between theoretical and experimental recurrence strength as a function of ϵ at constant values of S' for $m=0,1$. Quantum calculations are shown in gray and experimental data are in black. The $S'=9.5$, 14.5, and 16.5 curves show selected curves from the first sequence of recurrence maxima. The $S'=26.0$ and 40.0 curves are obtained from the second sequence of recurrence maxima, while the $S'=25.5$ graph shows a region of recurrence maxima in the third sequence.

spectrum of sodium in an applied field have been performed for $m=0,1,2$. The calculations use the known quantum defects of sodium and a Numerov integration routine to obtain the off-diagonal matrix elements of the atomic Hamiltonian in the field [6]. Only bound states with $n \leqslant 47$ are included in the calculation. Since no continuum levels are included, the simulation results are only strictly valid for energies below the classical saddle point, $\epsilon < -2$. The theoretical photoabsorption spectra are scaled in a manner identical to the experimental data and the corresponding recurrence spectra are displayed in Figs. 7(a) and 7(b). A weighted mixture of the different m values (32% $m=0$, 68% $m=1$ for the $m=0,1$ spectrum and 13.5% $m=0$, 29% $m=1$, 57.5% $m=2$ for the $m=2$ spectrum) is used to simulate the m state distribution in the experimental spectra. This distribution of m values is in reasonable agreement with the expected m state distributions from angular momentum coupling rules; 33% $m=0$, 66% $m=1$ for parallel polarization and 18% $m=0$, 27% $m=1$, and 55% $m=2$ for perpendicular polarization. A calculation of the Stark map of hydrogen (up to second order in the applied field) was also performed for $m=0$ and $m=2$, and scaled to obtain the hydrogenic recurrence spectra. These are presented in Fig. 8. The $m=2$ recurrence map for hydrogen closely matches both the theoretical and experimental $m=2$ spectra observed in sodium. This is to be expected due to the small quantum defect of the $\ell \geqslant 2$ states in sodium. While there are some similarities between the $m=0$ hydrogen recurrence map and the $m=0,1$ recurrence spectra for sodium, the agreement is not so pronounced.

B. The $m=0,1$ spectrum

The maxima in both the $m=0,1$ and the $m=2$ sodium scaled energy maps occur at or near the scaled actions corresponding to the crossing of the uphill and downhill orbits in the $m=0$ hydrogen scaled energy map. The description of the $m=0,1$ spectra is analogous to that presented by Courtney *et al.* in reference to their Li data [5]. In hydrogen, recurrence maxima lie along the repetitions of the primary ''uphill'' and ''downhill'' orbits (see Fig. 6). The strongest features correspond to bifurcations of these fundamental trajectories into other orbit types. However, in Na, the nonhydrogenic core allows scattering to occur directly between the fundamental uphill and downhill orbits. Maxima in the recurrence strength identify, primarily, combination orbits in which the electron precesses through a combination of uphill and downhill orbits. The static-field-induced modification of the Coulomb potential *increases* the period of the downhill motion while it *decreases* the period of the uphill motion. At the recurrence maxima, the ratios of the periods of the uphill and downhill motions are rational fractions (i.e., $i+j$ uphill orbits for every i downhill orbits). For $\epsilon < -2.5$, the changes in period of these fundamental orbits are nearly equal in

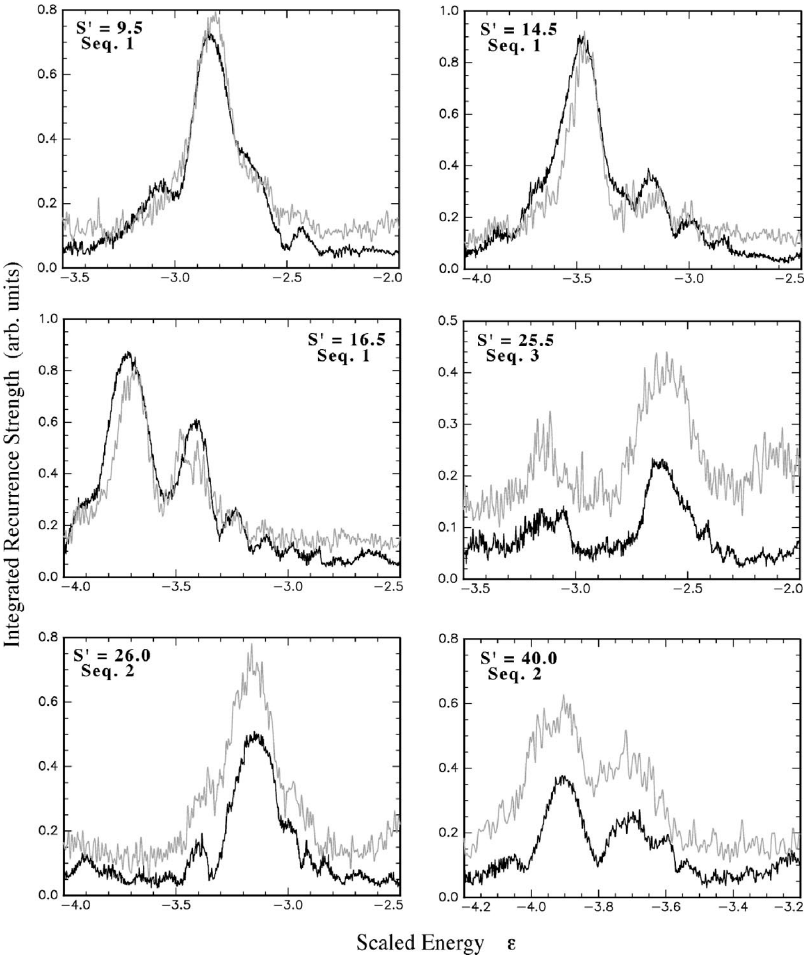

FIG. 11. Comparison between theoretical and experimental recurrence strength as a function of ϵ at constant values of S' for $m=2$. Quantum calculations are shown in gray and experimental data in black. Selected regions of scaled energies are shown for various scaled action values as described in Fig. 10.

absolute magnitude. Therefore, since the action variable S' acts as a Kepler orbit index, the action vs scaled energy curves for the $(i+j)$th uphill orbit and the ith downhill orbit should cross at a mean value $S'=i+j/2$. Indeed, the principal features in our $m=0,1$ spectra are found at integer and half-integer values of S' for $\epsilon<-2.5$.

C. The $m=2$ spectrum

Although the recurrence maxima for the $m=2$ spectra also occur at integer and half-integer values of S$'$, the underlying dynamics must be different, since the uphill and downhill orbits do not exist for $m\neq 0$ [14]. Nevertheless, the strong global patterns in the experimental and theoretical scaled maps must reflect the classical dynamics in these systems. Since the $m=2$ sodium and hydrogen spectra are essentially identical, we can make a classical interpretation of the spectrum by assuming a hydrogenic atom.

In weak applied fields, the Kepler period of radial motion, $\tau_K=2\pi n^3$, is significantly smaller than the Stark period, $\tau_s=2\pi/3Fn$. The Stark period identifies the time scale for the pendular motion of the major axis of the Kepler ellipse about the static field axis as well as the associated precession of the electron angular momentum [1]. Electrons that are launched from the core as $\ell=2$, $m=2$ Rydberg electrons travel away from the nucleus in, or near, the xy plane. If the applied field is weak, then the net angular momentum transfer per Kepler orbit due to the Stark field is small. So, after one Kepler period, there is a large probability that the electron will return to the nucleus on roughly the same trajectory with the same angular momentum. For a finite sized core, there is a range of initial launch angles which create trajectories that are not sufficiently deflected by the weak applied field to avoid being reincident upon the core after a single Kepler period. In scaled units, a weak applied field corresponds to low scaled energy, and therefore, for $\epsilon\lesssim-3$, there is a pronounced recurrence peak at very low scaled action corresponding to a single Kepler period (see Fig. 8). For lower ϵ there is an increasing probability that the electron will return to the nucleus before the Stark field can sufficiently affect the electron's orbit. With decreasing values of ϵ, the electron visits the core several times before its angular momentum increases to a level that prohibits its return to the nucleus. As a result, for $\epsilon<-4.0$ there are several maxima at small integer values of S'. In the limit of zero applied field, $\epsilon\rightarrow-\infty$ and $\tau_S\rightarrow\infty$, the electron returns to the nucleus after every Kepler orbit, leading to an infinite number of recurrence maxima at integer values of S'.

Note that there are fewer small action recurrence maxima in the $m=2$ data than in the corresponding $m=0$ recurrence spectra. An $\ell=2$, $m=2$ electron experiences a greater static-field-induced torque, $\tau=\vec{r}\times\vec{F}$, than the corresponding $m=0$ electron, since its orbit is essentially perpendicular to

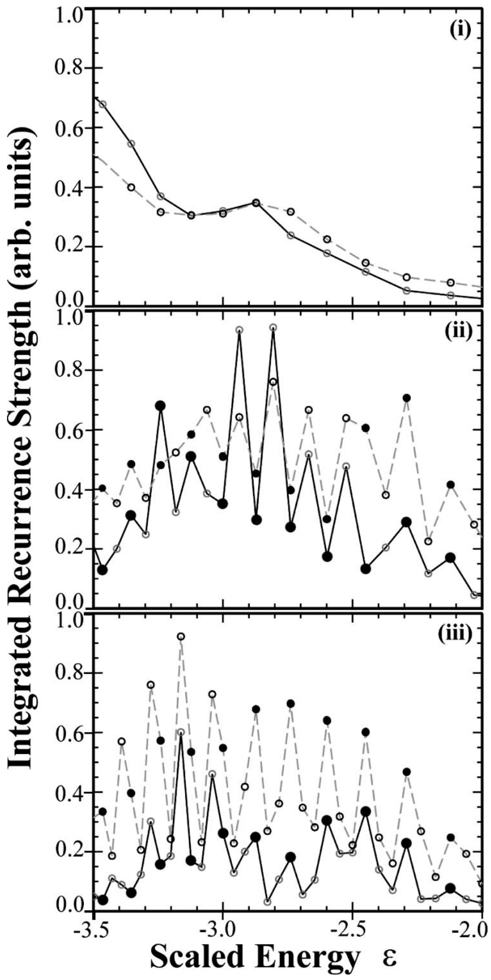

FIG. 12. Integrated recurrence strength as a function of average scaled energy for the first three sequences in $m=0,1$. Quantum calculations are indicated with dashed lines while experimental data are indicated with solid lines. Reducible orbits are indicated with filled circles while irreducible orbits are indicated with open circles. Note the periodicity of the strong features in the various sequences. The integrated recurrence strengths in each sequence are individually normalized to unity. However, a single normalization factor sets the relative amplitudes of the experiment and calculation in all three plots.

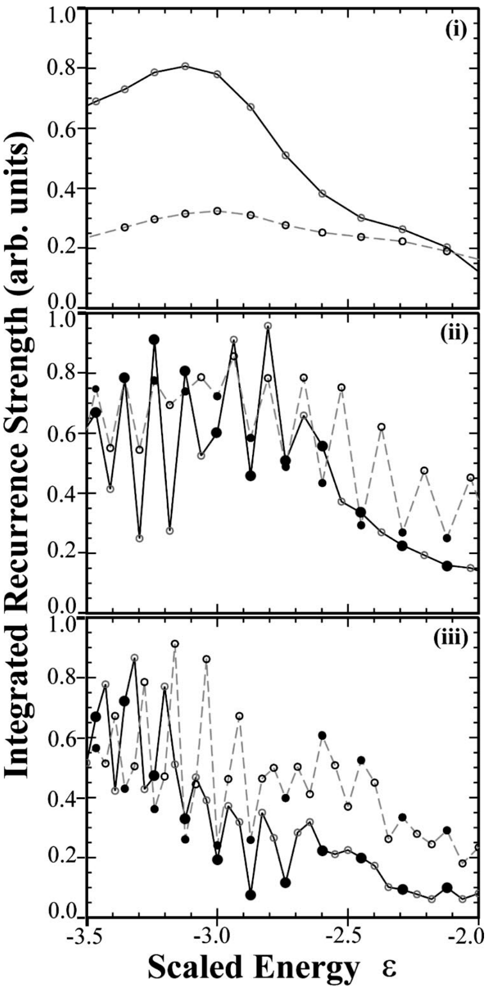

FIG. 13. Integrated recurrence strength as a function of average scaled energy for the first three sequences in $m=2$. Quantum calculations are indicated with dashed lines while experimental data are indicated with solid lines. Reducible orbits are indicated with filled circles while irreducible orbits are indicated with open circles.

the applied field. For orbits with a greater perpendicular component, $\Delta L/\Delta t$ is greater and the electron misses the core after fewer Kepler orbits due to its increased angular momentum.

After the initial recurrences in the $m=2$ map, there is a region of scaled action values without recurrence maxima. This empty region corresponds to times when the electron's orbit is precessing around the field axis through various angular momentum values. After a number of Kepler periods, determined by the launch angle and the scaled energy, the electron returns to the nucleus as indicated by a second region of strong recurrences. These recurrence maxima (sequence I) are located at an S' value that corresponds to the Stark period. During the first Stark period, the major axis of the Kepler ellipse completes one-half of a pendular cycle about the applied field axis while the electron angular momentum completes a full precessional cycle from low ℓ to high ℓ and back. When the electron returns to the core with low angular momentum at this time, the major axis of its orbit has precessed through an angle of approximately π. In essence, the pendular motion of the ellipse adds an extra half Kepler orbit to the motion. As a result, the return of the electron to the core (sequence 1 recurrence maxima) occurs at or very near a half-integer value of S'.

In a similar fashion, after another Stark period, the electron again returns to lower ℓ values and the nucleus, creating another region of recurrence maxima (sequence II) located at values of S' that are twice those of sequence I. At this time, the electron has completed two Stark periods and the major orbit of its axis has finished a full pendular cycle [1]. The returns to the nucleus occur after an integer number of primary Kepler orbits, and therefore the recurrence maxima are located at integer values of S'. Continuing in this manner, numerous sequences are observed in the recurrence spectrum, with the ith sequence corresponding to electrons that have completed i Stark periods.

For $\epsilon = -3.0$, recurrence maxima are observed for $S' = 10.5$, 11.5, 12.5, and 13.5, corresponding to $10\frac{1}{2}, 11\frac{1}{2}, 12\frac{1}{2}$, and $13\frac{1}{2}$ Kepler orbits, respectively. If we look at the second sequence, the range of Kepler orbits that contribute recurrence strength is larger, with significant recurrence maxima observed at $S' = 22$, 23, 24, 25, 26, and 27. In general, for a given value of ϵ, the higher the sequence number, the greater is the range of scaled actions that have significant recurrence strengths within a given sequence.

D. Global properties of the scaled energy maps

A comparison of the relative intensities of the individual recurrences within each sequence has also been performed. To facilitate the comparison, the recurrence map is binned in half-integer units of the action coordinate S' (see Fig. 9). This allows us to study several features of the scaled spectrum. First, we are able to investigate recurrence strengths at constant scaled actions S', as a function of scaled energy. Kips *et al.* [11] examined recurrence strength in this manner in their theoretical calculations; however, they were unable to compare their results to any experimentally measured spectra. Figure 10 shows recurrence maxima as a function of scaled energy for various values of S', showing both experimental data and quantum calculations for $m = 0,1$ in sodium. Figure 11 shows similar graphs for $m = 2$. A global shift in scaled energy of $\delta\epsilon = +0.03$ is applied to all the experimental data to obtain the best agreement between experiment and theory. Presumably, this small error is due to the uncertainty in the measurement of the applied electric field. The $S' = 26$ and $S' = 40$ graphs provide a view of a region of sequence II. The $S' = 25.5$ curve focuses on a region of sequence III. The curves in Figs. 10 and 11 are representative, and there is good overall agreement between data and theory, particularly in the first two sequences. Note that, aside from the slight shift in the experimental value of ϵ, there are no adjustable parameters in the calculation. A single normalization factor is used on the entire data set to allow comparison between experiment and theory.

Integrating the binned maps over a range of scaled energies yields the total recurrence strength for a given closed orbit as a function of sequence number. The recurrence strength value within ±10% of the center of each sequence is integrated to obtain the total recurrence strength per orbit per sequence. We define the center of the sequences as the crossing of the hydrogenic uphill and downhill repetition orbits (see Fig. 6). For the jth sequence and $\epsilon < -2.5$, the center is given approximately by the closed form expression for the crossing of the ith downhill repetition with the $(i+j)$th uphill repetition,

$$\epsilon_j(S') = \sqrt{\frac{3(S'+j/2)}{4j}}. \tag{6}$$

The resulting curves (see Figs. 12 and 13) represent integrated recurrence strengths as a function of scaled energy for each sequence. In general, each curve shows a modulation with a period of j Kepler orbits for a given sequence j. The integrated strength curves are sensitive to background noise in the recurrence map. As a result, the agreement between theory and experiment is only qualitative. Keeler and Morgan noticed similar structure within each sequence of integrated recurrence strength in their studies of helium [12]. They associated the oscillations with the types of orbit, reducible or irreducible, within each sequence. Our data, like those of Keeler and Morgan [12], exhibit strong definable modulations only over a limited range of scaled action. Figure 12 shows the integrated recurrence strength as a function of average scaled energy in the first three sequences for $m = 0,1$ theory and experimental data. Figure 13 shows the corresponding sequences for $m = 2$. Relative maxima and minima appear to be functions of whether the orbit in question is reducible or not; however, the functional dependence on whether reducible orbits correspond to relative maxima or to relative minima changes as a function of scaled action. In general, the scaled action values at which the crossovers occur are approximately the same as those at similar crossover features in He [12]. Also, the scaled action values at the crossovers in Na are the same in both the calculated and experimental spectra.

The observed periodicity is more evident in the $m = 0,1$ experimental data than in the corresponding $m = 2$ data. The lack of any such structure in the quantum calculation of the $m = 2$ sodium recurrence spectrum and the small quantum defect of the $m = 2$ states in sodium suggest that the presence of these features in the $m = 2$ experimental data is due solely to the presence of $m = 0,1$ states in the $m = 2$ spectra.

IV. SUMMARY

We have measured Na Stark maps as a continuous function of energy and applied static electric field. Using a modified set of scaled variables, the data are Fourier transformed to produce recurrence maps as a continuous function of scaled energy and scaled action. We have identified several global features of the recurrence map, including a propensity for recurrence strength to cluster at integer or half-integer values of the scaled action. Because of the continuous nature of the maps, we have been able to study with high resolution the recurrence strength as a function of scaled energy and scaled action.

Complicated modulations in the differential recurrence strength (strength vs scaled energy at fixed scaled action) and integrated recurrence strength (energy-integrated strength vs scaled action) that are observed in the data are in agreement with quantum simulations. It would be extremely interesting to determine at what level semiclassical methods can reproduce these structures. Theoretical investigations along these lines are currently underway [17].

ACKNOWLEDGMENTS

We would like to thank T. J. Bensky for his invaluable help in developing the data-collection software used in this experiment. This project is supported by the Packard Foundation and the AFOSR.

[1] T.P. Hezel, C.E. Burkhardt, M. Ciocca, L.-W. He, and J.J. Leventhal, Am. J. Phys. **60**, 329 (1992); T.P. Hezel, C.E. Burkhardt, M. Ciocca, and J.J. Leventhal, *ibid.* **60**, 324 (1992).

[2] T.W. Ducas, M.G. Littman, R.R. Freeman, and D. Kleppner, Phys. Rev. Lett. **35**, 366 (1975); T.F. Gallagher, L.M. Humphrey, R.M. Hill, and S.A. Edelstein, *ibid.* **37**, 1465 (1976); M.G. Littman, M.L. Zimmerman, T.W. Ducas, R.R. Freeman, and D. Kleppner, *ibid.* **36**, 788 (1976); M.G. Littman, M.M. Kash, and D. Kleppner, *ibid.* **41**, 103 (1978); M.L. Zimmerman, T.W. Ducas, M.G. Littman, and D. Kleppner, J. Phys. B **11**, L11 (1978); W.E. Cooke and T.F. Gallagher, Phys. Rev. A **17**, 1226 (1978); T.H. Jeys, G.W. Foltz, K.A. Smith, E.J. Beiting, F.G. Kellert, F.B. Dunning, and R.F. Stebbings, Phys. Rev. Lett. **44**, 390 (1980).

[3] L.D. Noordam, A. ten Wolde, A. Lagendijk, and H.B. van Linden van den Heuvell, Phys. Rev. A **40**, 6999 (1989); B. Broers, J.F. Christian, J.H. Hoogenraad, W.J. van der Zande, H.B. van Linden van den Heuvell, and L.D. Noordam, Phys. Rev. Lett. **71**, 344 (1993); B. Broers, J.F. Christian, and H.B. van Linden van den Heuvell, Phys. Rev. A **49**, 2498 (1994); G.M. Lankhuijzen and L.D. Noordam, *ibid.* **52**, 2016 (1995); Phys. Rev. Lett. **76**, 1784 (1996); J. Wals and H.B. van Linden van den Heuvell, J. Phys. B **30**, 941 (1997); M.T. Frey, F.B. Dunning, C.O. Reinhold, and J. Burgdorfer, Phys. Rev. A **55**, R865 (1997); C. Raman, T.C. Weinacht, and P.H. Bucksbaum, *ibid.* **55**, R3995 (1997); M.L. Naudeau, C.I. Sukenik, and P.H. Bucksbaum, *ibid.* **56**, 636 (1997); G.M. Lankhuijzen, F. Robicheaux, and L.D. Noordam, Phys. Rev. Lett. **79**, 2427 (1997); T.J. Bensky, M.B. Campbell, and R.R. Jones, *ibid.* **81**, 3112 (1998); M.B. Campbell, T.J. Bensky, and R.R. Jones, Phys. Rev. A **59**, R4117 (1999).

[4] H.A. Bethe and E.E. Salpeter, *Quantum Mechanics of One-and Two-Electron Atoms* (Plenum, New York, 1977); D.A. Harmin, Phys. Rev. A **24**, 2491 (1981); J.R. Rubbmark, M.M. Kash, M.G. Littman, and D. Kleppner, *ibid.* **23**, 3107 (1981); D.A. Harmin, Phys. Rev. Lett. **49**, 128 (1982); Phys. Rev. A **26**, 2656 (1982); F. Robicheaux and J. Shaw, Phys. Rev. Lett. **77**, 4154 (1996).

[5] M. Courtney, N. Spellmeyer, H. Jiao, and D. Kleppner, Phys. Rev. A **51**, 3604 (1995).

[6] M.L. Zimmerman, M.G. Littman, M.M. Kash, and D. Kleppner, Phys. Rev. A **20**, 2251 (1979).

[7] U. Eichmann, K. Richter, D. Wintgen, and W. Sandner, Phys. Rev. Lett. **61**, 2438 (1988).

[8] J. Gao and J.B. Delos, Phys. Rev. A **49**, 869 (1994).

[9] M. Courtney, H. Jiao, N. Spellmeyer, and D. Kleppner, Phys. Rev. Lett. **73**, 1340 (1994); M. Courtney, H. Jiao, N. Spellmeyer, D. Kleppner, J. Gao, and J.B. Delos, *ibid.* **74**, 1538 (1995).

[10] G.J. Kuik, A. Kips, W. Vassen, and W. Hogervorst, J. Phys. B **29**, 2159 (1996); A. Kips, W. Vassen, W. Hogervorst, and P.A. Dando, Phys. Rev. A **58**, 3043 (1998).

[11] A. Kips, W. Vassen, and W. Hogervorst, Phys. Rev. A **59**, 2948 (1999).

[12] M.L. Keeler and T.J. Morgan, Phys. Rev. Lett. **80**, 5726 (1998); Phys. Rev. A **59**, 4559 (1999).

[13] J.A. Shaw and F. Robicheaux, Phys. Rev. A **58**, 1910 (1998).

[14] F. Robicheaux and J. Shaw, Phys. Rev. A **58**, 1043 (1998).

[15] A.D. Peters, C. Jaffe, and J.B. Delos, Phys. Rev. Lett. **73**, 2825 (1994); P.A. Dando, T.S. Monteiro, and S.M. Owen, *ibid.* **80**, 2797 (1998).

[16] M.G. Littman, Opt. Lett. **3**, 128 (1978); M.G. Littman and H.J. Metcalf, Appl. Opt. **7**, 224 (1978).

[17] J. Shaw (private communication).